

Chao Yu

Key Laboratory for Mechanics in Fluid
Solid Coupling Systems,
Institute of Mechanics,
Chinese Academy of Sciences,
Beijing 100190, China

Yiwei Wang

Key Laboratory for Mechanics in Fluid
Solid Coupling Systems,
Institute of Mechanics,
Chinese Academy of Sciences;
School of Engineering Science,
University of Chinese Academy of Sciences,
Beijing 100190, China
e-mail: wangyw@imech.ac.cn

Chenguang Huang

Key Laboratory for Mechanics in Fluid
Solid Coupling Systems,
Institute of Mechanics,
Chinese Academy of Sciences;
School of Engineering Science,
University of Chinese Academy of Sciences,
Beijing 100190, China

Xiaocui Wu

Key Laboratory for Mechanics in Fluid
Solid Coupling Systems,
Institute of Mechanics,
Chinese Academy of Sciences,
Beijing 100190, China

Tezhuan Du

Key Laboratory for Mechanics in Fluid
Solid Coupling Systems,
Institute of Mechanics,
Chinese Academy of Sciences,
Beijing 100190, China

Large Eddy Simulation of Unsteady Cavitating Flow Around a Highly Skewed Propeller in Nonuniform Wake

Unsteady cavitating flows around propellers become increasingly prominent on large-scale and high-speed ships, but large eddy simulations (LES) are limited in the literature. In this study, numerical simulation of an unsteady cavitating flow around a highly skewed propeller in a nonuniform wake is performed based on an explicit LES approach with $k - \mu$ subgrid model, Kunz cavitation model, volume of fluid (VOF) method, and a moving mesh scheme are adopted. The predicted evolution of the unsteady cavitating flow around a highly skewed propeller in a nonuniform ship wake is in good agreement with experimental results. An analysis of the factors affecting the cavitation on the propeller is conducted based on numerical simulation. Furthermore, the influences between cavitation structures and vortex structures are also briefly analyzed. [DOI: 10.1115/1.4035218]

1 Introduction

The evolution of cavitation around the propeller in a nonuniform wake flow is a classic issue in the hydrodynamic field. Many difficulties are still encountered in solving this complex problem. Underwater cavitation and vortex motion are closely linked; thus, the turbulence model is one of the key components in the numerical simulation of cavitation flows.

For a long time, numerical simulations of cavitating flow are solved with Reynolds-averaged Navier–Stokes (RANS) turbulence models. For example, Watanabe et al. [1] simulated the unsteady cavitation on a propeller based on a RANS turbulence model and the Singhal cavitation model with the use of the commercial software FLUENT. The cavity shape and pressure fluctuations they predicted on the blade surfaces were fairly consistent with the obtained measurements. The application of the computational fluid dynamics (CFD) to the cavitating flow around a propeller in a nonuniform ship wake was discussed by Hasuiki et al. [2], who concluded that the RANS simulation could generate

valuable information for judging erosion risk, but its predictive accuracy and numerical stability are insufficiently good. Ji et al. [3,4] numerically simulated the propeller cavitation with the use of a shear stress transport turbulence model, a mass transfer cavitation model, and a sliding mesh approach; the predicted evolution of cavity and the pressure fluctuations on a propeller is in good agreement with experimental results. Furthermore, RANS turbulence models have been widely used in the numerical simulation of cavitation flows around other objects underwater [5–9]. Given that RANS turbulence models smooth a number of details of the turbulent movement, these methods have some limitations when simulating the effect of transient cavitation pulsation, whereas LES methods have performed better in this case.

Large eddy simulation methods are designed to simulate large-scale movements of unsteady vortex structures to more accurately simulate the transient characteristics of turbulence. In recent years, LES turbulence models are used to numerically simulate cavitation flow and achieved some progress; however, research on propeller cavitation is very limited. For example, Bensow and Bark [10,11] simulated unsteady cavitating flows around an INSEAN E779A propeller by implicit LESs. They predicted some important cavitation mechanisms, which were useful in assessing cavitation erosion, proved the validity of the method and pointed

Contributed by the Fluids Engineering Division of ASME for publication in the JOURNAL OF FLUIDS ENGINEERING. Manuscript received December 2, 2015; final manuscript received October 26, 2016; published online February 15, 2017. Assoc. Editor: Elias Balaras.

out that the LES of cavitation still needs further development and exploration. In addition, Lu et al. [12] adopted both LES and RANS simulation to simulate the cavitating flow on a marine propeller and compared simulation results with experimental results. They found that more refined bubble and vortex structures have been obtained in the LES-based simulation than in the RANS-based simulation. Then, Lu et al. [13] simulated the cavitating flow around two highly skewed propellers operating in open water and mounted on an inclined shaft by an approach based on incompressible LES combined with the VOF method to represent the liquid and vapor phases and the Kunz cavitation model. In their study, LES was demonstrated capable of capturing the mechanisms by comparing the LES results with experimental results. Furthermore, more promising results with refined bubble and vortex structures have been obtained using LES turbulence models to numerically simulate cavitation flows around other objects under-water [14–19].

To our knowledge, the numerical simulation of an unsteady cavitating flow around a propeller in a nonuniform wake with the use of an explicit LES approach has never been reported in the literature. Detailed results obtained using LES methods to simulate the propeller tip vortex cavitation are particularly limited. Much work is needed for a more comprehensive understanding of this issue. In this study, a numerical simulation of the cavitating flow around a highly skewed propeller in a nonuniform ship wake is performed based on an explicit LES approach with $k-\mu$ subgrid model. The Kunz cavitation model, the VOF method, and a moving mesh scheme are also adopted. Experimental [20,21] and numerical results are compared to prove the validity of the method. Furthermore, an analysis of the factors that affect the cavitation on the propeller is conducted based on the numerical simulation results. Influences between vortex structures and cavity structures are also briefly analyzed.

2 Numerical Simulation

2.1 Propeller Geometry and Flow Parameters. A scale model of the highly skewed propeller of “SEIUN-MARU” ship [20,21] is used in this study. The major specifications of the propeller are shown in Table 1. The propeller geometry model in the Cartesian coordinate system O - xyz is shown in Fig. 1. The x -axis corresponds to the propeller center rotation axis directed downstream, whereas the blade reference line (a straight line perpendicular to the axis of the propeller and used as a vertical reference line when drawing the blade) is taken as the z -axis (z is the direction of gravity). The y -axis obeys the right-hand rule, and the center point of the propeller is considered the coordinate origin. For simplicity of presentation, the angle θ between the z -axis and the propeller reference line indicates the blade position during rotation.

Parameters of this cavitating flow are drawn from previous experimental study literatures [20,21]. The rotational speed n is 17.5 rps. $K_T = \text{Thrust}/(\rho n^2 D^4) = 0.201$ represents the time-averaged thrust coefficient. The distribution of measured wake velocities is shown in Fig. 2. The cavitation number, $\sigma = (p_\infty - p_{\text{sat}})/(0.5\rho n^2 D^2)$, is 2.99, where $p_{\text{sat}} = 3450 P_a$ is the saturation vapor pressure of water.

2.2 Governing Equation and Cavitation Model. In cavitating flow around a propeller [3–4,10–13], the fluid is assumed to

Table 1 Principal parameters of propeller

Number of blades	5
Diameter at blade trip, D (m)	0.22
Pitch ratio	0.955 (at 0.7 R)
Skew angle ($^\circ$)	45
Rake angle ($^\circ$)	-3.03
Expanded area ratio	0.7
Blade section	Modified SRI-B

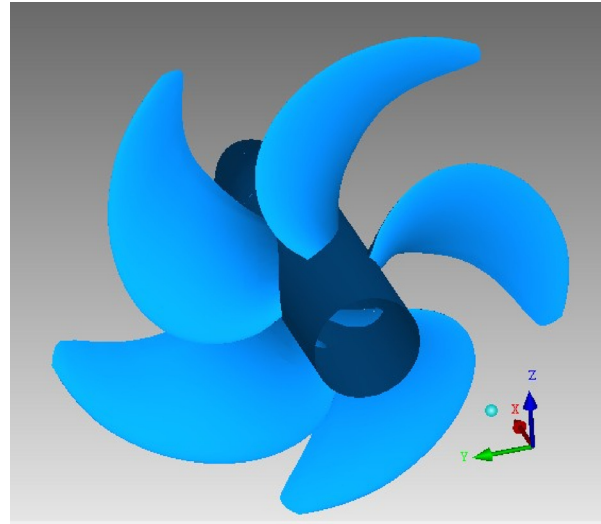


Fig. 1 Propeller geometry

be incompressible so that the numerical simulation is performed based on the incompressible Navier–Stokes equations as follows:

$$\begin{cases} \nabla \cdot (\rho \mathbf{v}) = 0 \\ \frac{\partial}{\partial t} (\rho \mathbf{v}) + \nabla \cdot (\rho \mathbf{v} \mathbf{v}) = -\nabla p + \nabla \cdot \mathbf{S} \\ \mathbf{S} = 2\mu \mathbf{D} \end{cases} \quad (1)$$

where ρ , \mathbf{v} , p , and μ are density, velocity, pressure, and viscosity coefficient of the mixture, respectively, and $\mathbf{D} = (1/2)(\nabla \mathbf{v} + \nabla \mathbf{v}^T)$ describes the strain rate tensor.

Large eddy simulation methods are used to simulate the turbulent flow. The basic idea of LES is that large-scale eddies are simulated by directly solving instantaneous Navier–Stokes equations, whereas small-scale eddies are reflected by the subgrid stress (SGS) model [22]. The SGS model and the filter function, which are used to distinguish large-scale from small-scale eddies, are the key components in the LES method. The spatial filtering averaging methods are as follows:

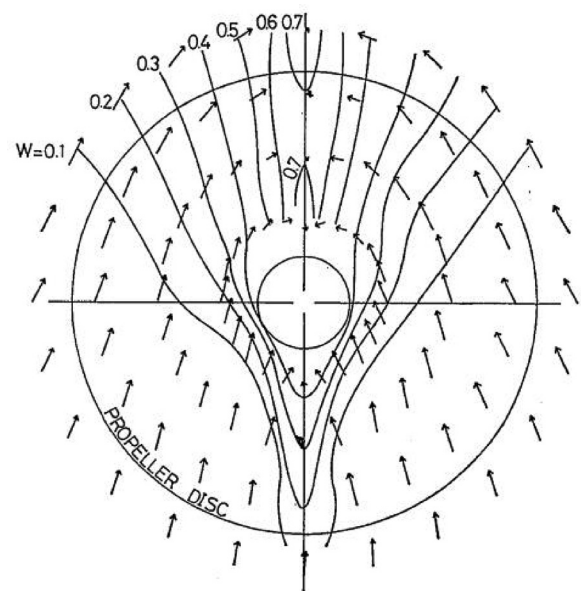


Fig. 2 Measured nominal wake distribution ($W_x = 1 - v_x/V_\infty$) [19]

$$\bar{u}_i(x) = \int G(|x - x'|) u_i(x) dx' \quad (2)$$

where $G(|x - x'|)$ is a filter function as well as a local function. In this paper, the box filter function is

$$G(|x - x'|) = \begin{cases} 1/\sqrt[3]{(\Delta_x \Delta_y \Delta_z)}, & |x_j - x'_j| \leq \frac{\Delta_j}{2}, j = x, y, z \\ 0, & |x_j - x'_j| > \Delta_j/2 \end{cases} \quad (3)$$

where Δ_j is the spatial filter size in direction j .

When the filter function is applied to Eq. (1), the following LES governing equations can be obtained

$$\nabla \cdot (\rho \bar{\mathbf{v}}) = 0 \quad (4)$$

$$\frac{\partial}{\partial t} (\rho \bar{\mathbf{v}}) + \nabla \cdot (\rho \bar{\mathbf{v}} \bar{\mathbf{v}}) = -\nabla \bar{p} + \nabla \cdot (\bar{\mathbf{S}} - \mathbf{B}) \quad (5)$$

where the over bar denotes the filtered physical quantity; $\mathbf{B} = \rho(\bar{\mathbf{v}} \bar{\mathbf{v}} - \bar{\mathbf{v}} \bar{\mathbf{v}})$ represents the influence of the small-scale eddies, meaning the SGS tensor.

On the basis of the Boussinesq hypothesis [23], a subgrid viscosity, μ_{sgs} , is considered to solve the SGS tensor. Consequently, the SGS tensor becomes

$$\mathbf{B} = -2\mu_{\text{sgs}} \bar{\mathbf{D}} \quad (6)$$

The subgrid viscosity μ_{sgs} is solved using the $k - \mu$ model [16,24]

$$\frac{\partial k_{\text{sgs}}}{\partial t} + \nabla \cdot (k_{\text{sgs}} \bar{\mathbf{v}}) = \nabla \cdot \left[\frac{\mu + \mu_{\text{sgs}}}{\rho} \nabla k_{\text{sgs}} \right] + 2 \frac{\mu_{\text{sgs}}}{\rho} \bar{\mathbf{D}} \bar{\mathbf{D}} - C_e \frac{k_{\text{sgs}}^{3/2}}{\bar{\Delta}} \quad (7)$$

$$\mu_{\text{sgs}} = C_k \bar{\Delta} \sqrt{k_{\text{sgs}}} \quad (8)$$

where k_{sgs} is the SGS turbulent kinetic energy, $\bar{\Delta} = \sqrt[3]{\Delta_x \Delta_y \Delta_z}$ is the average spatial filter size, $C_e = 1.048$, and $C_k = 0.094$.

A natural cavitation flow has two phases (liquid and vapor). The VOF approach, which α introduces the liquid volume fraction [25], is considered to describe both phases and the transition mechanism between them. In this approach, the mixture density and mixture viscosity of the fluid is defined as follows:

$$\rho = \alpha \rho_l + (1 - \alpha) \rho_v \quad (9)$$

$$\mu = \alpha \mu_l + (1 - \alpha) \mu_v \quad (10)$$

where ρ_l and ρ_v are the densities of liquid and vapor; μ_l and μ_v are the viscosities of liquid and vapor, respectively.

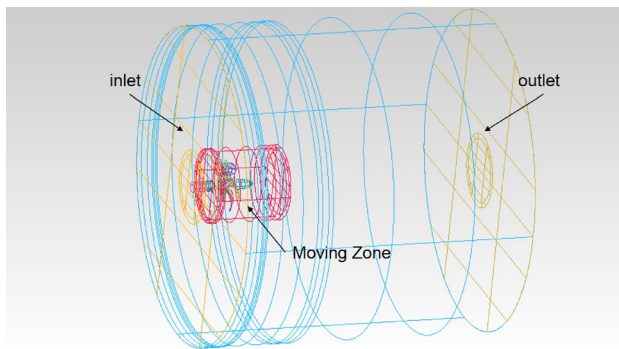


Fig. 3 Computation domain

Given the liquid volume fraction α , the following governing equations are derived:

$$\begin{cases} \frac{\partial \alpha}{\partial t} + \nabla \cdot (\bar{\mathbf{v}} \alpha) = \frac{\dot{m}}{\rho_l} \\ \nabla \cdot \bar{\mathbf{v}} = S_p \\ S_p = \left(\frac{1}{\rho_l} - \frac{1}{\rho_v} \right) \dot{m} \\ \frac{\partial}{\partial t} (\rho \bar{\mathbf{v}}) + \nabla \cdot (\rho \bar{\mathbf{v}} \bar{\mathbf{v}}) = -\nabla \bar{p} + \nabla \cdot (\bar{\mathbf{S}} - \mathbf{B}) \end{cases} \quad (11)$$

where \dot{m} is the mass transfer rate.

In the unsteady cavitation flow, the transition between liquid and vapor is complex. In this study, the mass transfer rate is based on the Kunz model [26]

$$\dot{m}^+ = \frac{C_v \rho_v \alpha \min[0, \bar{p} - p_v]}{(1/2 \rho_l U_\infty^2) t_\infty} \quad (12)$$

$$\dot{m}^- = \frac{C_c \rho_v \alpha^2 (1 - \alpha)}{t_\infty} \quad (13)$$

The evaporation rate \dot{m}^+ is proportional to the liquid volume fraction α and the amount of local pressure subtracting the saturated vapor pressure when the pressure is below the saturated vapor pressure. A third-order polynomial function of α is used to model the condensation rate \dot{m}^- . In Eq. (12), U_∞ is the speed of ship. The characteristic time, which is denoted by t_∞ is equal to D/U_∞ , where D is the diameter of the propeller. The empirical constants for the different phase transfer rates are denoted by C_v and C_c . These empirical constants are set to $C_v = 100,000$ and $C_c = 1000$, which are based on considerable computing experience.

2.3 Simulation Procedures. The numerical simulation is realized through the open source code OPENFOAM with the second-order implicit scheme for time discretization and Gauss linear upwind scheme for spatial discretization, which has been verified effective in simulation of cloud cavitating flow around a three-dimensional twisted hydrofoil by Wu et al. [24]. In order to reach a high accuracy in time, an adjustable time step is used with maximum Courant number (Co) of 0.5. The precise time steps are less than 5×10^{-6} s. To ensure that the flow is fully developed, the cavity results are coming from a propeller cycle after 0.4 s. The computational time is approximately 120 h for one revolution on 128 Intel Xeon E5620, 2.40 GHz central processing unit cores.

2.4 Computational Domain and Grids. The computational domain, as shown in Fig. 3, including a propeller, is drawn as recommended by Ji et al. [3,4]. The distance between the inlet plane and the propeller need to be treated prudently to keep the nonuniform wake in the propeller plane and avoid the negative effect on pressure field. When the distance between inlet plane and propeller plane is $0.7 D$, the wake distribution keeps well, as shown in Fig. 4. In the same time, the amplitude of fluctuation in y -direction caused by the inlet flow and propeller is less than 0.05, as shown in Fig. 5. The gradient of pressure coefficient in z -direction is mainly caused by gravity. Such effect on pressure field from the inlet is within an acceptable range. Thus, the domain inlet is located at $0.7 D$ upstream of the propeller, and the outlet is located at $5 D$ downstream of the propeller. Along the radial direction, the distance from the propeller axis to the cylindrical surface is $6 D$. The moving zone is a cylindrical region: $r/D \leq 0.6$, $x/D = [-0.3, 0.2]$. The interface between the moving zone and outer zone is treated as a split surface.

When the mesh is generated, the whole computational domain, as shown in Fig. 3, is mainly divided into the moving zone and the outer zone by the sliding surface. The outer zone has a

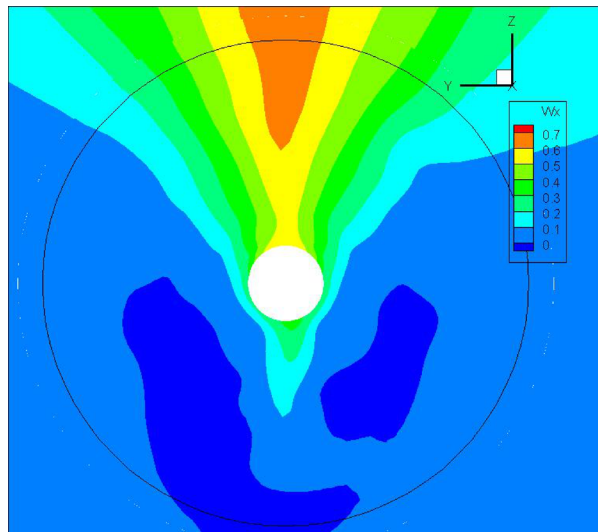


Fig. 4 Wake distribution at $0.3 D$ before the propeller plane

structured mesh with hexahedral cells. The moving zone has a multiblock mesh, which can be divided into four regions. As shown in Fig. 6, the region near the sliding surface and the region near the blade have high-quality structured grids. The blade tip and trailing region has a dense body. The remaining regions have unstructured meshes with tetrahedral cells. This kind of mixed structure mesh can improve the convergence rate and computational efficiency.

Considering the chord-based Reynolds number at $0.7R$ is $Re_{0.7R} = (0.7b_{0.7R}\pi nD/\nu) = 5.6 \times 10^5$, where $b_{0.7R}$ is the chord of the paddle at $0.7R$. At such a high Reynolds number, LES cannot resolve the eddies in the semiviscous near-wall region, unless a very fine mesh is used. The adoption of an approximate treatment which bridges the near-wall layer is necessary [27,28]. Thus, in this study, a wall model is used and the cell sizes in the wall normal direction are controlled in $y^+ < 50$ on the propeller. For the surface mesh, the length of $x^+, z^+ < 200$ is encountered in the middle of the blade with considerably smaller rectangles used toward the edges. This near-wall resolution is deemed sufficient for reliable wall-modeled LES based on our experiences with the applied wall model.

Mesh independence should be examined to guarantee calculation accuracy. An additional simulation is performed by using a

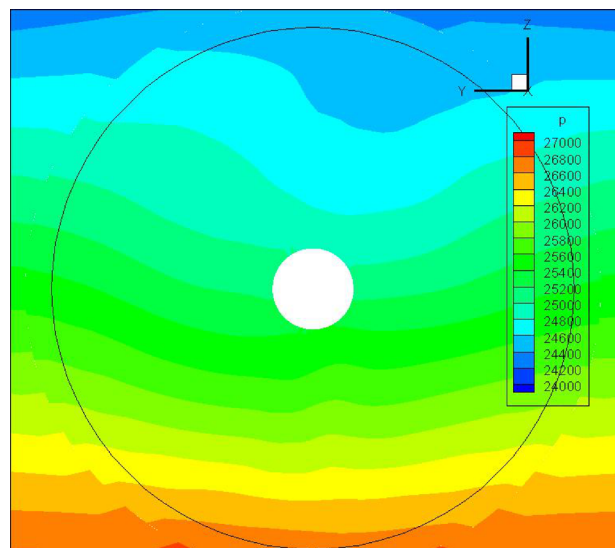
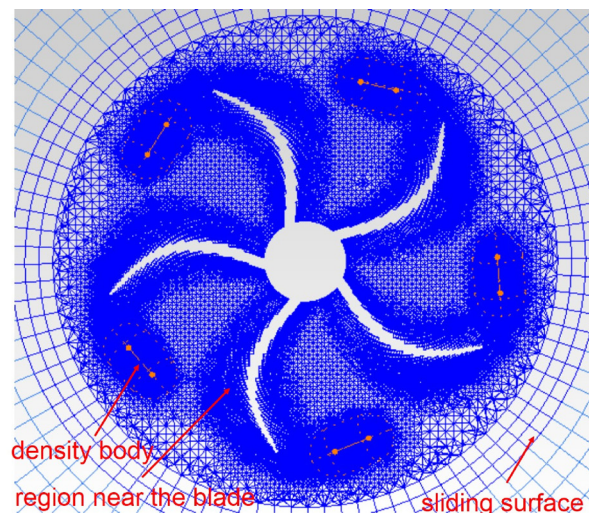


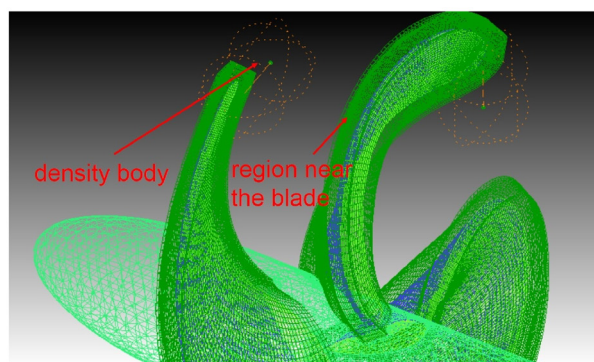
Fig. 5 Pressure distribution at $0.3 D$ before the propeller plane

coarse grid with 1.8×10^6 cells. In Table 2, the cavity formations and evolution are similar with various meshes, while more details of tip vortex cavitation at $\theta = 0$ deg, 40 deg, 60 deg are captured by using the fine mesh. Thus, taking account of computational resources and accuracy together, the fine grid is used in this case.

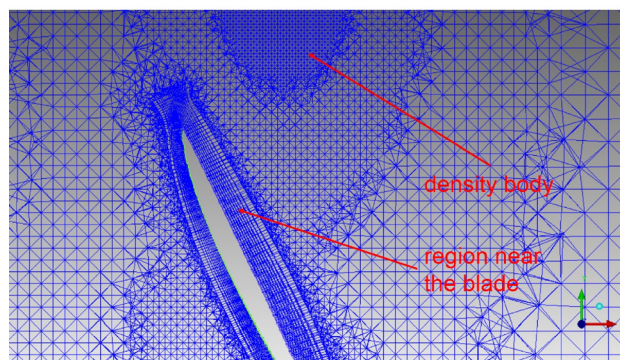
2.5 Boundary Conditions. The boundary of inlet is fixed velocity. The distribution of velocity on the inlet plane is consistent with the wake flow as shown in Fig. 2, where $V_\infty = 2.79$ m/s is computed from $K_T = 0.201$. The boundary of outlet is fixed pressure, where $P_\infty = 25,700$ Pa is calculated from $\sigma = 2.99$. The condition of the slip surface is cyclic Arbitrary Mesh Interface (cyclicAMI), which was introduced in OpenFOAM 2.1.0



(a)











(b)



(c)

Fig. 6 Details of the element layout: (a) is the section of $X = 0$ and (c) is the section of $Z = 0.3 D$

Table 2 Cavity shape with different mesh number

	$\theta = 0^\circ$	$\theta = 20^\circ$	$\theta = 40^\circ$	$\theta = 60^\circ$
Coarse mesh				
Fine mesh				

[29] to enable simulation across disconnected, adjacent, mesh domains for nonconformal patches [30]. This approach is particularly useful for rotating geometries, and more discussions on the effectiveness can be found in Ref. [31].

3 Results and Discussion

3.1 Overall Evolution of the Cavity. The evolution of the cavity pattern from the simulation is compared with the

experimental data obtained by Kurobe et al. [20] and Takahashi [21] to validate the present numerical method, as shown in Fig. 7. In the simulation, we use the isosurface of vapor fraction with $\alpha_v = 0.1$ to illustrate the cavity shape. When the cavity appears at $\theta = 350$ deg, the isosurface of vapor fraction with $\alpha_v = 0.001$ is used to capture the cavitation inception.

Figure 7 shows eight snapshots of the cavity shape against the position angle $\theta = 350(-10) \sim 60$ deg in increment of 10 deg. When the blade rotates in the wake zone, at $\theta = 350$ deg, the

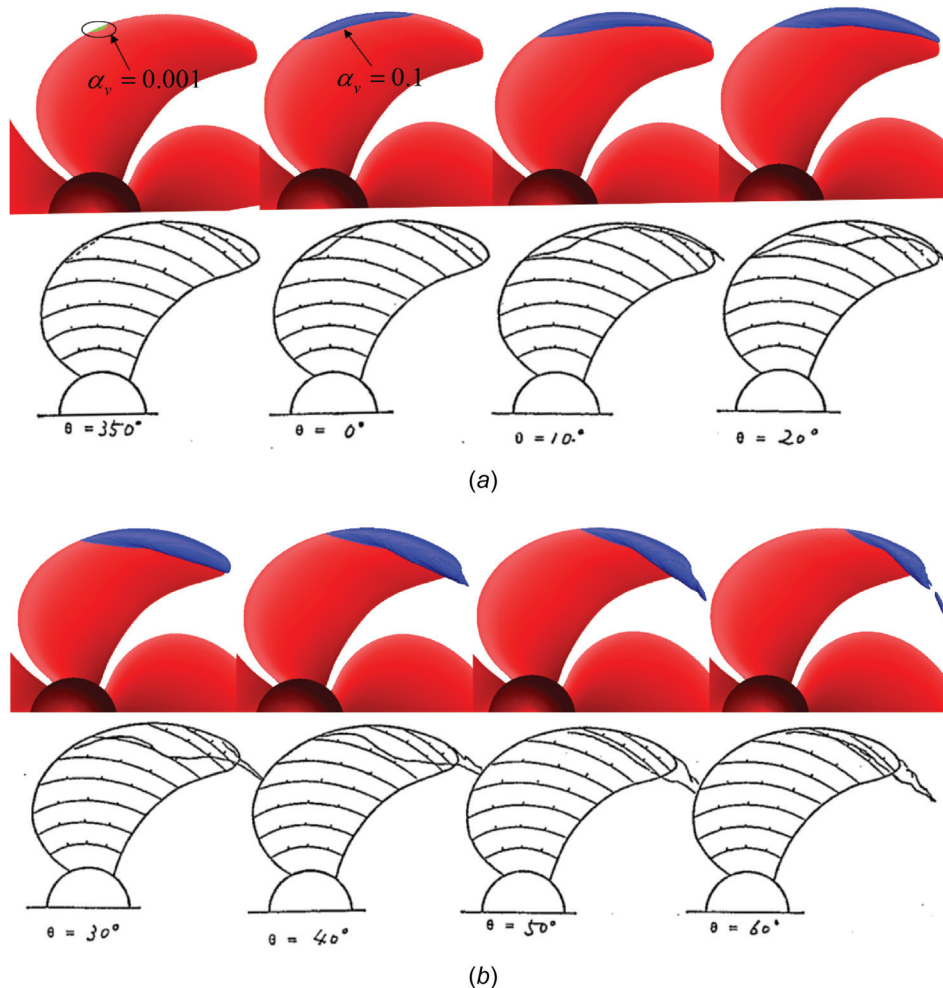


Fig. 7 Evolution of the cavity pattern during propeller rotation. (Numerical results are in the first and third row, while experimental results are in the next row.)

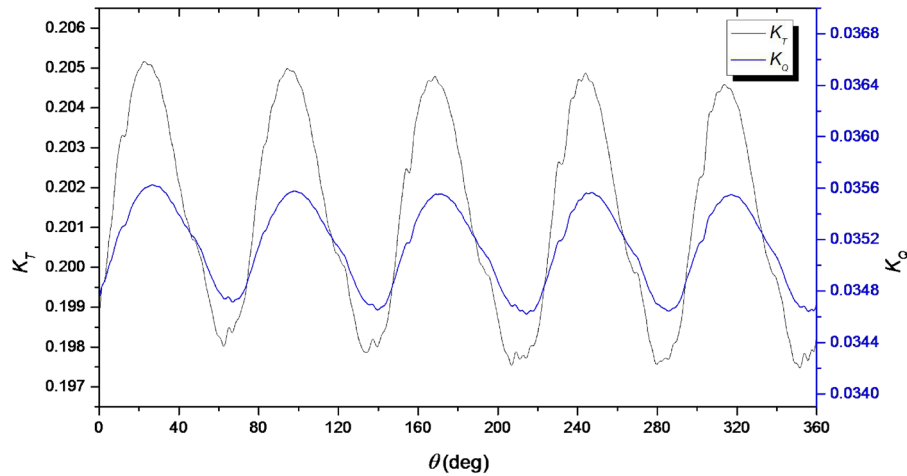


Fig. 8 Variations of thrust coefficient and torque coefficient in numerical results. (The thrust coefficient is presented by the black line with the left label, while the torque coefficient is presented by the blue line with the right label.)

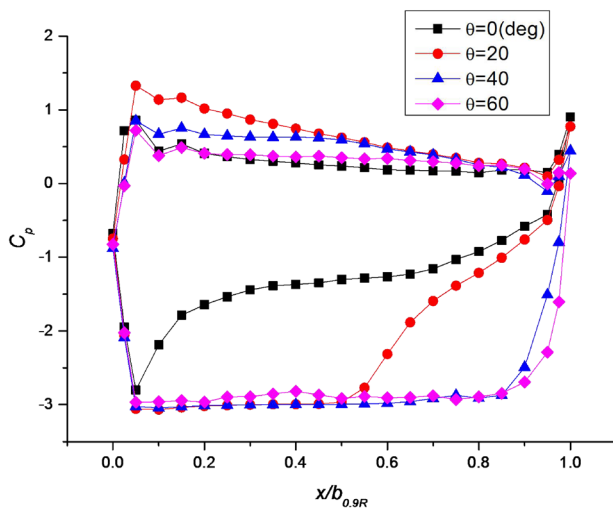


Fig. 9 The distributions of C_p on the section of blade at $0.9 R$. ($b_{0.9R}$ is the chord of blade at $0.9 R$, $C_p = (p - p_\infty) / (0.5 \rho n^2 D^2)$ is pressure coefficient.)

cavity appears from the middle of the blade leading edge and then develops downstream. Subsequently, the tip vortex cavity appears and the forepart of the cavity shrinks toward the tip after $\theta = 30$ deg. These phenomena are reasonably reproduced in the numerical results, especially the cavitation inception and the cavity shape after $\theta = 40$ deg.

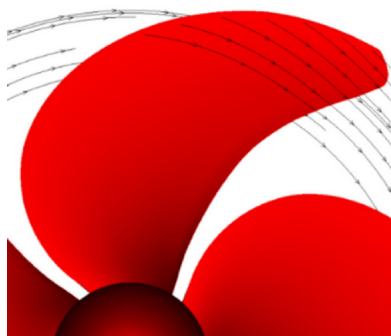


Fig. 10 Streamline near a blade

However, there are still several differences between numerical and experimental results. For example, tip cavities are not captured clearly at $\theta = 20$ deg, 30 deg and also smaller in following snapshots in numerical results, which represents that the resolution of the tip vortex is not satisfied yet. The numerical scheme and mesh discretization need to be further improved in the future.

3.2 Characteristics of Pressure. Variations of thrust coefficients $K_T = \text{thrust} / (\rho n^2 D^4)$ and torque coefficients $K_Q = \text{torque} / (\rho n^2 D^5)$ over one propeller rotational cycle are displayed in Fig. 8. The time-averaged thrust coefficient $K_T = 0.201$ is the same as experiments. In one propeller rotational cycle, K_T and K_Q both have five cycles corresponding to the number of blades. High-frequency fluctuations appear on both of the K_T and K_Q lines in the range of $\theta = 60 \sim 70$ deg because of the pressure fluctuation caused by cavity shedding.

The pressure distributions on the section of blade at $0.9 R$ at different angles were shown in Fig. 9. On the leeside of the blade, they have the same value of low pressure, about $C_p = -2.99$, after the leading edge. But the region of the low pressure is different between various angles. Corresponding to the cavity on section $0.9 R$, as shown in Fig. 3, the length of the low pressure region after the leading edge is the same as cavity. At $\theta = 0$ deg, the regions of both low pressure and cavity are the least. At $\theta = 20$ deg, the regions of both low pressure and cavity are

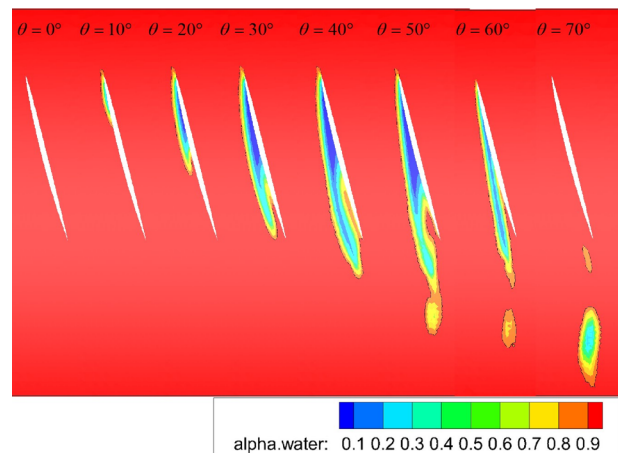


Fig. 11 Variations of cavity shape on cylindrical section $0.9 R$

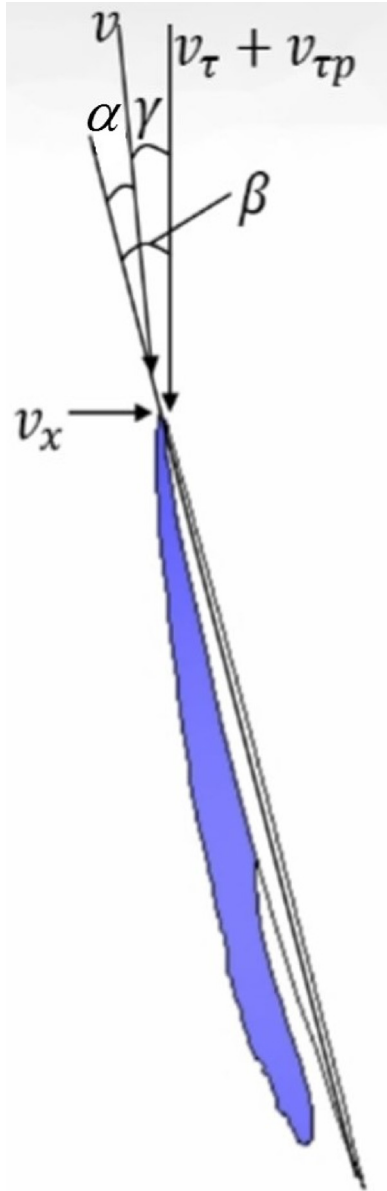


Fig. 12 Influencing factors of the cavity on cylindrical sections. (The relative flow velocity v is composed of the relative rotational linear velocity $v_{r,p} = 2\pi nr$, where r is the distance to rotation axis, the wake flow velocity which mainly includes tangential velocity v_τ and the axial velocity v_x . The attack angle α is an angle between the relative flow velocity and the section of the blade and $\alpha = \beta - \gamma$, where β is the pitch angle of the blade and γ is the angle between the tangential direction and relative flow velocity.)

$x/b_{0.9R} \leq 0.55$. At $\theta = 40$ deg, 60 deg, the regions of both low pressure and cavity are almost covered all the length of chord.

3.3 Influencing Factors of Cavitation Evolution. The factors affecting cavitation evolution are worth studying when the blades rotate in the wake zone. In the simulated flow, the streamlines near the blade tip tend to be along the circumference, as shown in Fig. 10. Thus, the influencing factors of cavitation evolution could analyze from the perspective of the cylindrical sections. The cavitation evolution in the cylindrical section, as shown in Fig. 11, has many similarities with the cavitation in the hydrofoil [32], including growth, recirculating, shedding, and collapse processes. Similar to the factors in hydrofoil cavitation, the factors

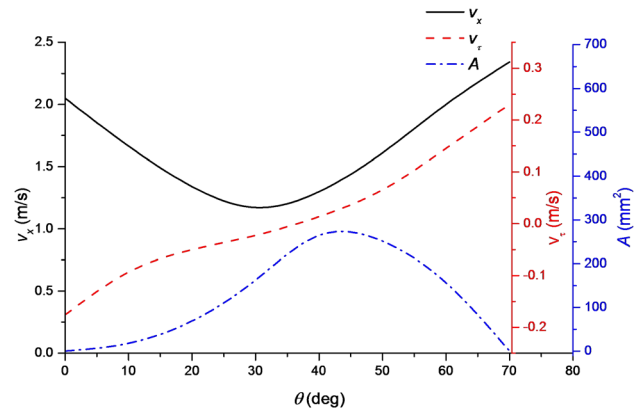


Fig. 13 Variations of axial velocity v_x and tangential velocity v_τ comparing with the area of cavity on section $0.9R$. (The axial velocity is presented by the black line with the left label, the tangential velocity is presented by the red line with the center label, and the cavity area is presented by the blue line with the right label. The axial velocity and tangential velocity are captured from the point on the plane $0.3D$ before the propeller plane corresponding to the center point on the chord.)

that affect the cavitation in the blade are the relative flow velocity magnitude v and the attack angle α , as shown in Fig. 12.

To determine the influencing factors of cavitation evolution clearly, a simple x - y line plot of cavity area comparing with the axial velocity v_x and tangential velocity v_τ is described in Fig. 13. From the trends of those curves, there is a significant positively correlation between v_x and cavity area. The misalignment between the peaks of v_x and cavity area is mainly caused by the influence of v_τ . After v_x reaching a peak, the growth of cavity area is mainly caused by the increase of v_τ . Thus, the cavity area is positively related to v_x and negatively related to v_τ . And the cavity area is mainly influenced by v_x .

Considering the influence of pitch angle β , the attack angle α of the relative velocity need to be calculated out. From Fig. 14, the relative velocity magnitude of the flow around the blade is $U = \sqrt{(v_x^2 + (v_\tau + v_{tp})^2)}$. Thus, a local cavitation index can be defined as $\sigma_t = (p_\infty - p_{sat}) / (0.5\rho(v_x^2 + (v_\tau + v_{tp})^2))$. Variations of local cavitation index σ_t and attack angle α comparing with the area of cavity are described in Fig. 15. From the trends of those curves, there is a significant positively correlation between α and cavity area. When $\theta \leq 30$ deg, σ_t decrease slowly. At this stage,

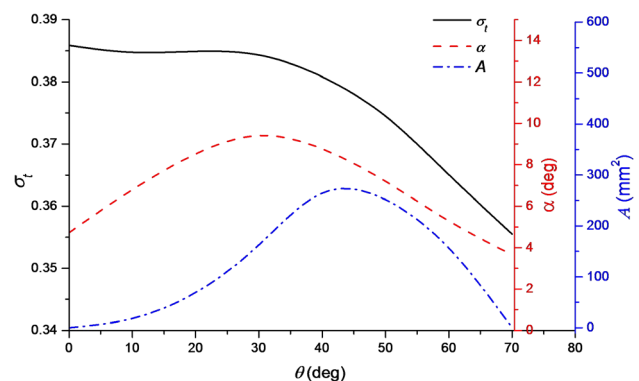


Fig. 14 Variations of the local cavitation index (σ_t) and the attack angle (α) comparing with the cavity area (A) on section $0.9R$. (The local cavitation index is presented by the black line with the left label, the attack angle is presented by the red line with the center label, and the cavity area is presented by the blue line with the right label).

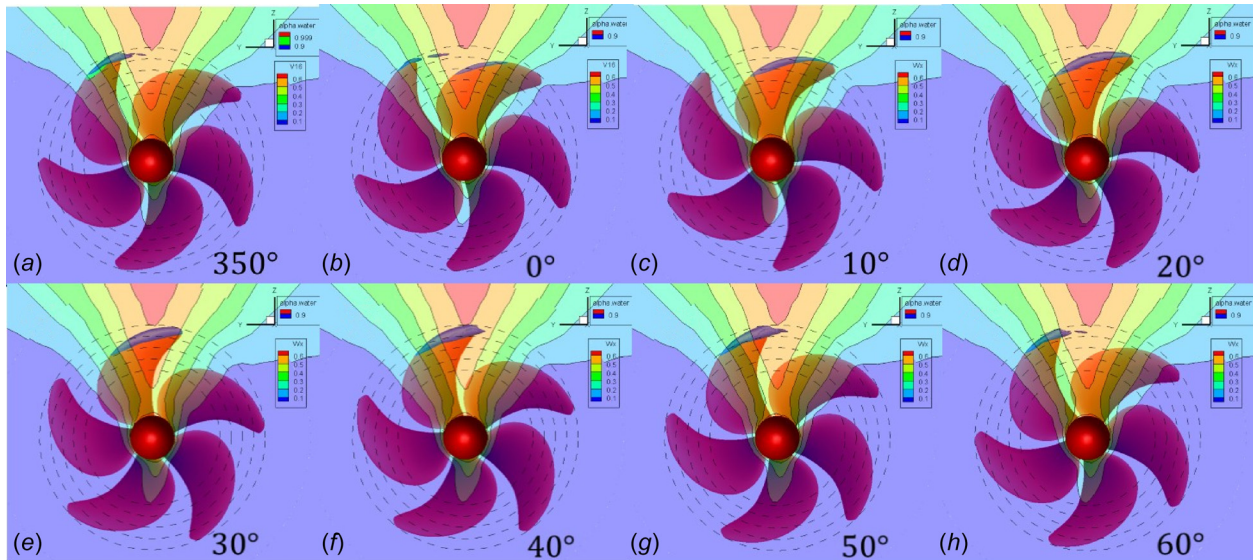


Fig. 15 The wake flow axial velocity distribution and cavity ($X = -0.15 D$)

the increase of cavity area is mainly caused by the increase of α . When $30 \text{ deg} \leq \theta \leq 40 \text{ deg}$, after α reaching a peak, the growth of cavity is mainly caused by the decrease of σ_t . When $\theta > 45 \text{ deg}$, the cavity area decreased because of the decrease of α . Thus, the cavity area is negatively related to σ_t and positively related to α . And the cavity area is mainly influenced by α . As $\alpha = \beta - \gamma$, cavity area is positively related to β . As v_{tp} is the main components of relative flow velocity, cavity area is positively related to v_{tp} .

From the analysis above, the cavity develops with the increasing of v_t , v_{tp} , and β but shrinks with the increasing of v_x . Also, this can be verified in the analysis of characteristics of regional distribution of cavity in the wake flow.

Given that the cavity shrinks with the increasing of v_x , the cavity appears only when the blade is rotating in the wake zone, where $W_x \geq 0.2$, as shown in Fig. 15. When the blade is rotating at the center of the wake zone, with the v_x decreasing, the cavity develops, as shown in Figs. 15(a)–15(d). When the blade is rotating away from the center of the wake zone, as shown in Figs. 15(e)–15(h), with the v_x increasing, the cavity shrinks.

As shown in Fig. 16, cavity region in left is larger than right on circle $r = 0.9R$. As those factors of v_x , v_{tp} , and β are symmetrical, the asymmetrical cavity region is caused by the tangential wake velocity v_t , which is larger in the left region than right as shown in Fig. 17.

Moreover, v_{tp} proportionally increase with so that cavitation easily appears in the place near the tip.

On the basis of the presented analyses, cavitation can be eliminated by two methods. The first way is to adjust the wake flow such as through additional hydrofoils. The other method is to

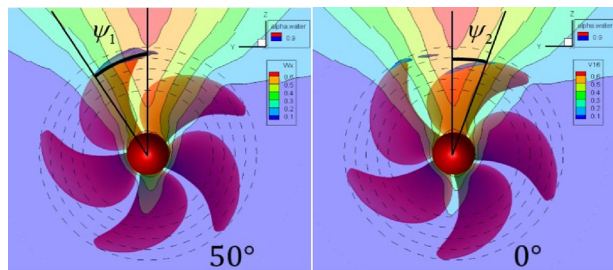


Fig. 16 Cavity region on circle $d = 0.9 D$ (ψ_1, ψ_2 are the cavity region in the left and right on circle $d = 0.9 D$, respectively)

change the pitch angle when the blade is rotating in the wake zone. For example, a composite propeller could change the pitch angle under different conditions because of the properties of its materials and structures.

3.4 Analysis of Cavitation Structures and Vortex Structures. In the complex cavitating flow around a highly skewed propeller in nonuniform wake, the influencing factors of cavity evolution are more complex than the analysis above. In which, the vortex structure is also a key factor worth analyzing. Given that cavity and vortex motion are closely linked, the analysis of vortex structures and cavitation structures is necessary.

In this paper, vortex structure is represented by Q -criterion [33]. In incompressible flow, Q is defined as

$$Q = \frac{1}{2} (\|\Omega\|^2 - \|D\|^2) \quad (14)$$

where $\Omega = (1/2)(\nabla \mathbf{v} - \nabla \mathbf{v}^T)$ represents the vorticity tensor and $D = (1/2)(\nabla \mathbf{v} + \nabla \mathbf{v}^T)$ represents the strain rate tensor.

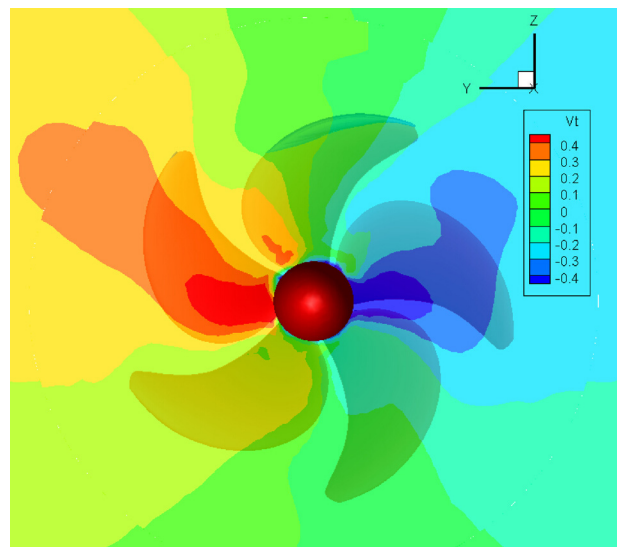


Fig. 17 The wake flow tangential velocity distribution ($X = -0.15 D$)

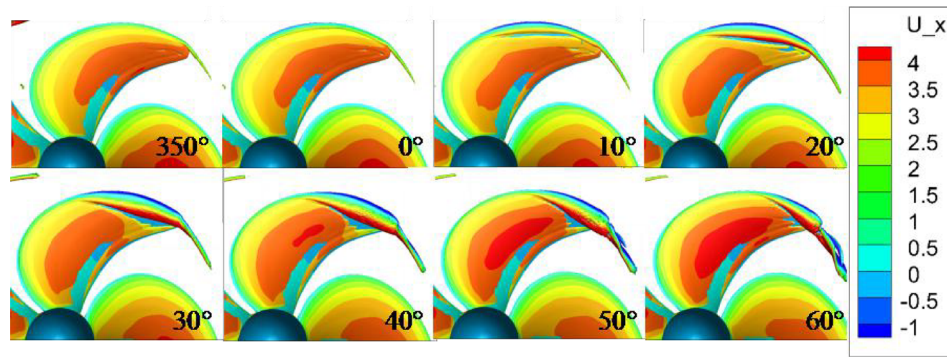


Fig. 18 Vortex structures ($Q = 500,000 \text{ s}^{-2}$)

Q has a direct physical meaning. When $Q > 0$, the vector field is dominated by the vorticity and the region is determined as a vortex tube. When $Q < 0$, the vector field is dominated by the strain. This physical interpretation supports the value of Q -criterion in the vector fields when areas of high strain and areas of strong vortical motions should be distinguished.

In Fig. 18, the isosurfaces of $Q = 500,000 \text{ s}^{-2}$ reflect the vortex structures. Compared with the cavity shapes in Fig. 7, the vortex structures and cavitation structures almost have identical shapes. They are mainly of two kinds. When $\theta < 30$ deg, cavities and vortices mainly occur near the leading edge which are long and thin. When $\theta > 30$ deg, the sheet cavitation and vortices is dominated, which are unstable with cloud cavitation emerging at the closure. The cavitation and vortices influence each other.

On the one hand, viscosity significantly influences vortex motions. According to Eq. (10), the mixture viscosity is proportional to α , the liquid volume fraction. Thus, the cavitation region with lower mixture viscosity and smaller eddy dissipation is beneficial to the strong vortex motions.

On the other hand, the pressure is lower in the vortex tube; thus, the cavity is easy to form inside and around it. The cavity will also tend to gather at the vortex center.

Therefore, when $\theta = 10$ deg, 20 deg, 30 deg, the relatively stable leading edge vortex, which is long and thin, leads to the formation and development of the filamentous tip vortex cavitation. By contrast, when $\theta = 40$ deg, 50 deg, 60 deg, the sheet cavitation structures, which have a collapsed cavity and a cloud cavitation at the tip, lead to the broken of tip vortex structures and formation of mixed vortex structures which form numerous filamentous vortices.

4 Conclusions

In this study, an unsteady cavitating turbulent flow around a highly skewed propeller in a nonuniform wake is simulated based on LES method, Kunz cavitation model, VOF method, and a moving mesh scheme. The predicted evolution of the unsteady cavity around the propeller in the nonuniform wake flow is in good agreement with the experimental results. Some pressure characteristics on the propeller are analyzed with the cavity.

In addition, a brief analysis of the factors affecting the cavitation on the propeller is conducted using the numerical simulation results. Through the analysis of influencing factors on the cylindrical section $0.9R$, we conclude that the cavity develops with the increasing of v_z , v_{tp} , and β but shrinks with the increasing of v_x . It is also verified in the analysis of characteristics of regional distribution of cavity in the wake flow.

Furthermore, the influences between vortex structures and cavitation structures are analyzed. Cavitation and vortex motion are closely linked. The cavitation region with a smaller mixture viscosity is beneficial to the formation of an area with strong vortical motions. In the vortex tube, the pressure is smaller; as a result, the cavitation is easily formed.

When $\theta < 30$ deg, because of the strong leading edge vortex structure, the cavity maintains relatively stable near the leading edge and begin to form a filamentous tip vortex cavitation. When $\theta > 30$ deg, a sheet cavitation occurs, which is unstable and transforms to cloud cavitation at the closure induced by the re-entry jet.

However, much work has yet to be done to simulate unsteady cavitating flows around propellers. The shedding of the tip vortex cavitation could not be captured clearly when the tip vortex cavitation is too slim. This phenomenon may be because the grid in the trailing region of the blade tip is insufficiently detailed, thereby affecting the accuracy of the tip vortex cavitation. What's more, to simulate the cavity around the propeller more accurate, a joint simulation by both considering the propeller and the ship model is needed in the future.

Acknowledgment

The authors are grateful to the Science and Technology Innovation Project of Chinese Academy of Sciences through Grant No. KGFZD-125-014, National Natural Science Foundation of China through Grant Nos. 11202215 and 11332011, and the Youth Innovation Promotion Association of CAS (2015015).

References

- [1] Watanabe, T., Kawamura, T., Takekoshi, Y., Maeda, M., and Rhee, S. H., 2003, "Simulation of Steady and Unsteady Cavitation on a Marine Propeller Using a RANS CFD Code," *Fifth International Symposium on Cavitation*, Osaka, Japan, Nov. 1–4, Paper No. GS-12-004.
- [2] Hasuike, N., Yamasaki, S., and Ando, J., 2009, "Numerical Study on Cavitation Erosion Risk of Marine Propellers Operating in Wake Flow," *7th International Symposium on Cavitation*, Ann Arbor, MI, Aug. 17–22, Paper No. 30.
- [3] Ji, B., Luo, X., Peng, X., Wu, Y., and Xu, H., 2012, "Numerical Analysis of Cavitation Evolution and Excited Pressure Fluctuation Around a Propeller in Non-Uniform Wake," *Int. J. Multiphase Flow*, **43**, pp. 13–21.
- [4] Ji, B., Luo, X., Wang, X., Peng, X., Wu, Y., and Xu, H., 2011, "Unsteady Numerical Simulation of Cavitating Turbulent Flow Around a Highly Skewed Model Marine Propeller," *ASME J. Fluids Eng.*, **133**(1), p. 011102.
- [5] Ying, C., and Lu, C. J., 2008, "A Homogenous-Equilibrium-Model Based Numerical Code for Cavitation Flows and Evaluation by Computation Cases," *J. Hydrodyn., Ser. B*, **20**(2), pp. 186–194.
- [6] Decaix, J., and Goncalves, E., 2013, "Compressible Effects Modeling in Turbulent Cavitating Flows," *Eur. J. Mech. B-Fluids*, **39**, pp. 11–31.
- [7] Goncalves, E., 2011, "Numerical Study of Unsteady Turbulent Cavitating Flows," *Eur. J. Mech. B-Fluids*, **30**(1), pp. 26–40.
- [8] Wang, Y., Liao, L., Du, T., Huang, C., Liu, Y., Fang, X., and Liang, N., 2014, "A Study on the Collapse of Cavitation Bubbles Surrounding the Underwater-Launched Projectile and Its Fluid-Structure Coupling Effects," *Ocean Eng.*, **84**, pp. 228–236.
- [9] Huang, B., Young, Y. L., Wang, G., and Shyy, W., 2013, "Combined Experimental and Computational Investigation of Unsteady Structure of Sheet/Cloud Cavitation," *ASME J. Fluids Eng.*, **135**(7), p. 071301.
- [10] Bensow, R. E., and Bark, G., 2010, "Simulating Cavitating Flows With LES in Openfoam," *Fifth European Conference on Computational Fluid Dynamics*, J. C. F. Pereira, and A. Sequeira, eds., Lisbon, Portugal, pp. 14–17.
- [11] Bensow, R. E., and Bark, G., 2010, "Implicit LES Predictions of the Cavitating Flow on a Propeller," *ASME J. Fluids Eng.*, **132**(4), p. 041302.
- [12] Lu, N. X., Svennberg, U., Bark, G., and Bensow, R., 2012, "Numerical Simulations of the Cavitating Flow on a Marine Propeller," *8th International Symposium on Cavitation*, Claus-Dieter OHL, eds., Singapore, pp. 338–343.

- [13] Lu, N. X., Bensow, R. E., and Bark, G., 2014, "Large Eddy Simulation of Cavitation Development on Highly Skewed Propellers," *J. Mar. Sci. Technol.*, **19**(2), pp. 197–214.
- [14] Wang, G., and Ostoja-Starzewski, M., 2007, "Large Eddy Simulation of a Sheet/Cloud Cavitation on a NACA0015 Hydrofoil," *Appl. Math. Model.*, **31**(3), pp. 417–447.
- [15] Liu, D. M., Liu, S. H., Wu, Y. L., and Xu, H. Y., 2009, "LES Numerical Simulation of Cavitation Bubble Shedding on ALE 25 and ALE 15 Hydrofoils," *J. Hydrodyn., Ser. B*, **21**(6), pp. 807–813.
- [16] Yu, X., Huang, C., Du, T., Liao, L., Wu, X., Zheng, Z., and Wang, Y., 2014, "Study of Characteristics of Cloud Cavity Around Axisymmetric Projectile by Large Eddy Simulation," *ASME J. Fluids Eng.*, **136**(5), p. 051303.
- [17] Ji, B., Luo, X. W., Arndt, R. E., Peng, X., and Wu, Y., 2015, "Large Eddy Simulation and Theoretical Investigations of the Transient Cavitating Vortical Flow Structure Around a NACA66 Hydrofoil," *Int. J. Multiphase Flow*, **68**, pp. 121–134.
- [18] Huang, B., Zhao, Y., and Wang, G., 2014, "Large Eddy Simulation of Turbulent Vortex-Cavitation Interactions in Transient Sheet/Cloud Cavitating Flows," *Comput. Fluids*, **92**, pp. 113–124.
- [19] Wang, Y., Huang, C., Fang, X., Yu, X., Wu, X., and Du, T., 2016, "Cloud Cavitating Flow Over a Submerged Axisymmetric Projectile and Comparison Between Two-Dimensional RANS and Three-Dimensional Large-Eddy Simulation Methods," *ASME J. Fluids Eng.*, **138**(6), p. 061102.
- [20] Kurobe, Y., Ukon, Y., Koyama, K., and Makino, M., 1983, "Measurement of Cavity Volume and Pressure Fluctuations on a Model of the Training Ship SEIUN-MARU With Reference to Full Scale Measurement," Ship Research Institute, Technique Report No. (NAID) 110007663078.
- [21] Takahashi, H., 1984, "Full Scale Measurements on Training Ship 'SEIUN-MARU,'" 17th International Towing Tank Conference (ITTC 84), O. Rutgersson, eds., SSPA, Sweden, pp. 323–334.
- [22] Nicoud, F., and Ducros, F., 1999, "Subgrid-Scale Stress Modelling Based on the Square of the Velocity Gradient Tensor," *Flow Turbul. Combust.*, **62**(3), pp. 183–200.
- [23] Schmitt, F. G., 2007, "About Boussinesq's Turbulent Viscosity Hypothesis: Historical Remarks and a Direct Evaluation of its Validity," *C. R. Méc.*, **335**(9), pp. 617–627.
- [24] Wu, X. C., Wang, Y. W., and Huang, C. G., 2016, "Effect of Mesh Resolution on Large Eddy Simulation of Cloud Cavitating Flow Around a Three Dimensional Twisted Hydrofoil," *Eur. J. Mech. B-Fluids*, **55**(Pt. 1), pp. 229–240.
- [25] Passandideh-Fard, M., and Roohi, E., 2008, "Transient Simulations of Cavitating Flows Using a Modified Volume-of-Fluid (VOF) Technique," *Int. J. Comput. Fluid Dyn.*, **22**(1–2), pp. 97–114.
- [26] Kunz, R. F., Boger, D. A., Stinebring, D. R., Chyczewski, T. S., Lindau, J. W., Gibeling, H. J., and Govindan, T. R., 2000, "A Preconditioned Navier–Stokes Method for Two-Phase Flows With Application to Cavitation Prediction," *Comput. Fluids*, **29**(8), pp. 849–875.
- [27] Temmerman, L., Leschziner, M. A., Mellen, C. P., and Fröhlich, J., 2003, "Investigation of Wall-Function Approximations and Subgrid-Scale Models in Large Eddy Simulation of Separated Flow in a Channel With Streamwise Periodic Constrictions," *Int. J. Heat Fluid Flow*, **24**(2), pp. 157–180.
- [28] De Villiers, E., 2007, "The Potential of Large Eddy Simulation for the Modelling of Wall Bounded Flows," Ph.D. thesis, University of London, London.
- [29] OpenFOAM Foundation, 2011, "Arbitrary Mesh Interface," *OpenFOAM Foundation, London*.
- [30] Farrell, P. E., and Maddison, J. R., 2011, "Conservative Interpolation Between Volume Meshes by Local Galerkin Projection," *Comput. Methods Appl. Mech. Eng.*, **200**(1), pp. 89–100.
- [31] Mehdi-pour, R., 2013, "Simulating Propeller and Propeller-Hull Interaction in OpenFOAM," *M.Sc. thesis*, Centre for Naval Architecture Royal Institute of Technology, Stockholm, Sweden.
- [32] Leroux, J. B., Coutier-Delgosha, O., and Astolfi, J. A., 2005, "A Joint Experimental and Numerical Study of Mechanisms Associated to Instability of Partial Cavitation on Two-Dimensional Hydrofoil," *Phys. Fluids*, **17**(5), p. 052101.
- [33] Sahner, J., Weinkauff, T., and Hege, H. C., 2005, "Galilean Invariant Extraction and Iconic Representation of Vortex Core Lines," *EUROGRAPHICS-IEEE VGTC Symposium on Visualization*, Leeds, UK, pp. 151–160.